HAL open science

# Angular modeling of a rotating machine in non-stationary conditions: Application to monitoring bearing defects of wind turbines with instantaneous angular speed

Jose L. Gomez, Ilyes Khelf, Adeline Bourdon, Hugo André, Didier Rémond

▶ **To cite this version:**

Jose L. Gomez, Ilyes Khelf, Adeline Bourdon, Hugo André, Didier Rémond. Angular modeling of a rotating machine in non-stationary conditions: Application to monitoring bearing defects of wind turbines with instantaneous angular speed. Mechanism and Machine Theory, 2019, 136, pp.27 - 51. 10.1016/j.mechmachtheory.2019.01.028 . hal-03485905

**HAL Id: hal-03485905**

**https://hal.science/hal-03485905v1**

Submitted on 20 Dec 2021

**HAL** is a multi-disciplinary open access archive for the deposit and dissemination of scientific research documents, whether they are published or not. The documents may come from teaching and research institutions in France or abroad, or from public or private research centers.

L'archive ouverte pluridisciplinaire **HAL**, est destinée au dépôt et à la diffusion de documents scientifiques de niveau recherche, publiés ou non, émanant des établissements d'enseignement et de recherche français ou étrangers, des laboratoires publics ou privés.

Distributed under a Creative Commons Attribution - NonCommercial 4.0 International License

Version of Record: https://www.sciencedirect.com/science/article/pii/S0094114X18315489
Manuscript_a2e3b98b5a589758950d1bb07efb02ce

# Angular modeling of a rotating machine in non-stationary conditions: application to monitoring bearing defects of wind turbines with Instantaneous Angular Speed

Jose L. Gomez[a], Ilyes Khelf[a,b,*], Adeline Bourdon[a], Hugo André[c], Didier Rémond[a]

[a] *Univ Lyon, INSA-Lyon, CNRS UMR5259, LaMCoS, F-69621, France.*
[b] *ENGIE GREEN, France*
[c] *Univ Lyon, UJM-St-Etienne, LASPI, EA3059, F-42023 Saint-Etienne, France*

**Abstract**

This work has been developed within the framework of non-stationary rotating machinery surveillance with emphasis on the detection of rolling element bearing defects. The numerical models proposed in this paper are based on an "angular" approach which introduces explicitly the machine's free body rotation degrees of freedom allowing simulations in non-stationary operating conditions. In a previous work, a deep groove ball bearing model has been presented considering the rolling resistance phenomena, allowing to describe the angular speed variations due to the bearing dynamics, a phenomenon that has been detected experimentally. In this work, a classic gear mesh description together with the rolling element bearing defects model have been used to build a wind turbine virtual machine. The model is used as a device to test Instantaneous Angular Speed spectral indicators. .

*Keywords:* Dynamic model, angular appraoch, wind turbine, instantaneous angular speed, condition monitoring, bearings, gear.

## 1. Introduction

Simulation models have been used to deepen the understanding of the physical phenomena. In the domain of rotating machinery surveillance, models are useful to analyze the real systems under different operating conditions, to test signal processing methods as well as new detection and prognosis techniques.

*Corresponding author
*Email addresses:* jlgc60@gmail.com (Jose L. Gomez), ilyes.khelf@insa-lyon.fr (Ilyes Khelf), adeline.bourdon@insa-lyon.fr (Adeline Bourdon), hugo.andre@univ-st-etienne.fr (Hugo André), didier.remond@insa-lyon.fr (Didier Rémond)



© 2019 published by Elsevier. This manuscript is made available under the CC BY NC user license
https://creativecommons.org/licenses/by-nc/4.0/

The modeling of the dynamics of rolling element bearings has been in constant development since the first half of the nineteenth century. Depending on the objective of the research, some works are dedicated to mathematically describing the experimental response of the bearing while others are based in the theoretical analysis of the mechanical component interaction. In the first group, the aim is to simply generate signals to be used as a tool for testing signal processing and detection methods. One comprehensive work in this context, was presented by Mc Fadden and Smith [1] in which the bearing dynamics was described in terms of time frequency equations, taking into account the kinematics of the bearing leading to the characteristic frequencies. In the same context Brie [2] proposes a different approach in which an analytical expression is presented modeling the bearing impulse with time-varying parameters. The model has been tested with different numerical simulations illustrating an inner race defect. One last example can be found in [3] where the authors model the defect as a series of short impulses occurring with a frequency inherent to the bearing characteristic frequency. This kind of approaches are only suitable to produce simulated signals that can be tuned to emulate specific dynamic behavior but they do not allow to describe the variation of magnitude of the load that is applied to the bearings, which is accentuated when the operating condition changes.

Within the group of works in which the dynamics of the rolling element is taken into account we find the one developed by Sawalhi and Randall [4]. The model takes into account the nonlinearity resulting from estimating the rolling element normal forces by means of the theory of Hertz which is translated into nonlinear varying stiffness related to the rolling element displacements. Localized defects may be added to the inner race (IR), the outer race (OR) and the rolling elements. One of the limitations of this approach is that it was developed for a constant rotational speed of the inner race. The bearing model was tested and assembled to a lumped parameter model of a gear stage and shafts to build a numerical representation of a test rig.

In a previous work, Gomez et al [5] presented a model as an extension of the Sawalhi and Randall's approach. The angular approach was used to build a model in which consideration of the inner race rotation degree of freedom (DOF) allows simulations of non stationary conditions as well as the Instantaneous Angular Speed (IAS) phenomenon.

The finite element method has also been applied to the modeling of the rolling dynamics in stationary conditions. Singh et al [6] obtained a very good correlation between the simulation results and experimental ones. The laboratory tests were carried on a test rig with a fairly simplified kinematics. The model shows a high level of detail, and the modeling parameters have to be tuned to allow realistic simulation over a reasonable time. Nevertheless, the application of this type of modeling on more complex kinematics remains a challenge facing the need for information for completely identifying each system, tuned simulation parameters, and a high computational complexity.

Regarding the gear interaction, its modelling is about the description of the flexible coupling and the excitation sources introduced into the mechanical

system by the interacting gears. Usually, the gear excitation is described as the non linear teeth mesh stiffness, the transmission error due to teeth imperfections. Almost two decades ago, Özgüven and Houser [7] published an extensive review of the different modeling approaches for gear coupled systems. Here we describe some recent publications which give context to the current work.

In [8], Bartelmus proposed an approach of multi-body modeling to represent one driving motor, one gear stage comprised of two gears and two shafts, and one driven machine as mechanical bodies. The approach for linking the multiple bodies is by external connecting forces. The equations of motion, obtained from the application of the Newton's second law for each body consider three DOF: two radial displacements and the angular rotation which comprehends the rigid body motions. The supports are modeled as linear forces of stiffness and damping applied to the bodies. The gear interacting or connecting forces are obtained as the result of modeling the tooth mesh as a spring and a damper "attached" to both of the gear base circles. The dynamic gear mesh force of the gears is a function depending on several variables representing the interacting tooth stiffness, the tooth deformation and the transmission errors.

In a further work, Bartelmus et al. [9, 10] tested the model described above in different configurations (two-stage, three-stage and a planetary transmission) under varying load configurations. The machines were considered to work in intervals of constant speed depending on the load to build defect simulated indicators that were compared to experimental ones.

With a different approach for the gearing excitations, Velex and Ajmi [11] performed the modeling in pure torsion and then considered three DOF of a one stage helical test rig to present an approach of gearing excitations by means of the combination of static and dynamic transmission errors. As the angular speed is considered constant the angular DOF $\theta$ is made equal to $\Omega \cdot t$ where $\Omega$ represents the speed of the driving shaft.

The model of Sawalhi and Randall [4] coupled the bearing and gearing interaction by modeling a single-stage gear test rig with lumped parameters with a total of 34 DOF taking into account the bearings and the casing. The pair of meshing gears are modeled as two cylindrical masses connected by an angular dependent stiffness combined with excitations taking into account the tooth deviations and misalignment. Gears have three DOF each: two translations plus the angular rotation. However, this model considers only a constant angular speed of the input shaft.

Nowadays, the increasing number of industrial applications demanding for non stationary machines (e.g. wind turbines, airplanes, automotive transmissions, etc.), has been a catalyst for the improvement and the development of existing models in order to enhance conventional condition monitoring tools. The difficulty with the typical analysis tools in presence of non-stationary regimes is that it causes spectral smearing and frequency modulation which hide the defects on the spectral domain complicating detection, analysis and prognosis of faults. In the angular domain, all cyclic phenomena are directly related to the rotation of the shafts of the inspected machine and the dependency with time

and ergo with speed is no longer an issue. In this work, the angular modeling approach is adopted which allow to have the angular degree of freedom as an explicit output of the system.

The objective of the present work is to model a whole wind turbine dynamics. An optimal level of abstraction and detail must be found in order to have a global model representative of a quite wide range of machines, taking into account realistic non-stationary conditions induced by wind speed variation and to provide global indicators whose trend of evolution are realistic enough. The model helps to understand the effects of the appearance of bearing defects on the instantaneous angular speed fluctuations of rotating shafts.

Different sizes of defect were considered to simulate a realistic defect level evolution. At the same time, IAS signals were extracted from an industrial wind turbine under defective bearing condition and after bearing replacement. The same constructed indicators on simulated signals were extracted, and evolution trends compared.

The rest of the paper is organized as fellows :Section 2 introduces the angular modeling approach based on Finite Element Method considering, shafts with 6 DOFs (three rotations and three displacements), advanced bearing modeling and an adjustment of classical assumptions for gear mesh modeling.
Section 3 sees the construction of a simplified model of a real wind turbine, The model simulating IAS measurements is used then for the construction of relevant fault indicators. In Section 4 simulated signals as well as the evolution of trends in the level of the indicators are analyzed and compared to experimental ones, in order to evaluate the effectiveness of modeling approach. Section 5 concludes the paper and give some future perspectives.

## 2. General modelling approach

In current approach, illustrated in figure 1, the mechanical system is divided into "structural elements" such as shafts and supports, "linking elements" such as bearings, gears or engines and external loads.
Structural elements are discretized into nodes with 6 DOFs as defined in equation 1, Let X be the vector containing the generalized displacements of the nodes describing the system.

$$[X]_{nod} =^T [x \quad y \quad z \quad \theta_x \quad \theta_y \quad \theta_z]_{nod} \tag{1}$$

In the presented work the shaft's axial rotation is in the direction of the axis z.
Structural elements are modeled using mass $[M]$, stiffness $[K]$ and damping $[C]$ matrices. The internal damping was handled in the same way as it was in

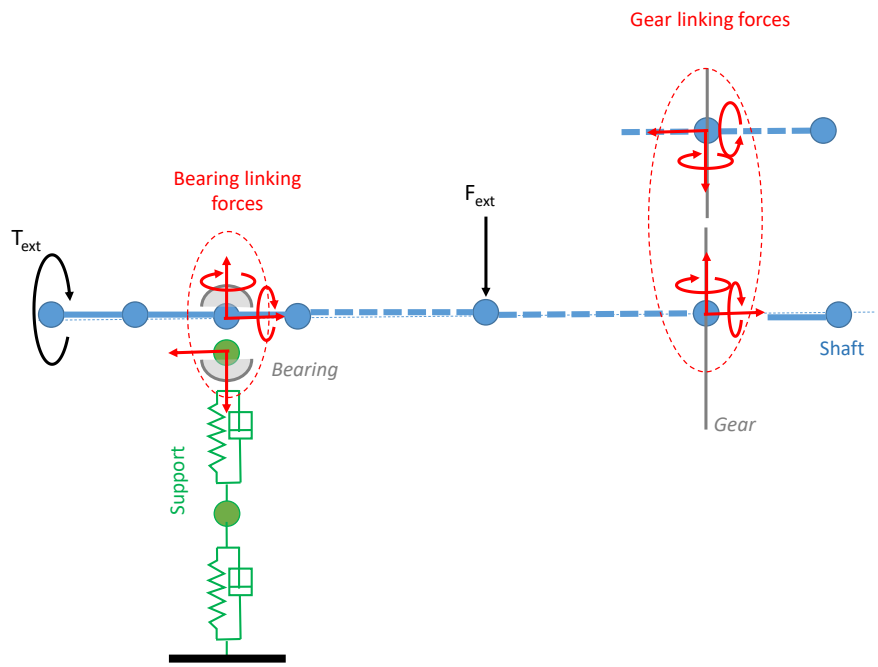


Figure 1: General modelling approach

Gomez et al. [5]. Shafts are modeled using Timoshenko beams and some lumping parameters may be added. The supports may be described by an approach of lumping parameters or by means of reduced finite element 3D models. Effects of "linking elements" are introduced as inner loads applied on the nodes of the structural elements. Values of these loads depend inter alia of displacements X of the connecting nodes and are computed for each iterations. Details are given in the following. These linking loads are gathered into vector $F_{link}$. External loads can be constant or time depend, are applied on nodes and are gathered into vector $F_t$.

All the elements are assembled into the general differential system (equation 2):

$$[M] \cdot [\ddot{X}] + [C][\dot{X}] + [K][X] = [F_{ext}(t)] + [F_{link}(X)] \tag{2}$$

Proposed approach allows to compute dynamic response of the mechanism but does not make it possible to calculate its eigenmodes. Nevertheless, if necessary eigenfrequencies could be identified by frequency analysis of a transitory signal.

### 2.1. The angular approach

The angular approach is based on two elements: the former is the fact that the angular degree of freedom $\theta_z$ is explicitly an output of the system. The second is that the shafts are allowed to turn freely along the axial direction meaning that the rigid body modes are not suppressed from the system's response.

Consideration of the angular DOFs implies that viscoelastic damping in $\theta_z$, or rigid body angular damping $\nu$ has to be considered to reach the steady state condition. This parameter represents the set of mechanical losses of the system in rotation and it may be concentrated on one node of the shaft or it may be distributed into all the angular DOFs of the finite elements describing the shaft. In Appendix A is illustrated the effect of this damping in a system of one degree of freedom. Notice that the steady state angular speed of the system is a function of this damping and it can be used to adjust the desired operating conditions of a given mechanical model. Throughout this work the rigid body angular damping is equally distributed through all the Finite elements.

### 2.2. The rolling element bearing models

As it was said in the introduction, modelling the rolling bearings is about the estimation of the linking forces between the shafts and the supports (See Figure 1). Two different approaches are simultaneously used in this paper: the first uses the Palmgren equations to find the linking forces as a function of the displacements of the nodes representing the inner and the outer races of the bearing. In the second approach, the dynamics of each rolling element is taken into account and variation of the IAS is introduced by means of the rolling resistance phenomenon. The second approach is used to precisely model defective bearing while the first one is used to speed up the computation of background healthy bearings. $[F_{bea}]$ contains the linking forces for all the bearings. The assembly is made following the finite element connectivity used for modelling the structural elements.

#### 2.2.1. Adapted Palmgren formulation for the estimation of the rolling bearing linking forces

The equations of Palmgren [12] describe a way for the estimation of the radial and axial relative displacements of the bearings' races $\delta_r$ and $\delta_a$ as a function of the load applied. In this work, we use the equations to estimate the bearing radial load as a function of the displacements. We present the equations for the deep groove ball bearing (DGBB) and the cylindrical roller bearings as a function of the number of rolling elements $Z$, the effective contact length $La$ (for cylindrical bearings) and the rolling element diameter $Dw$ (for DGBB).

$$\text{DGBB:} \quad F_{pal} = \frac{Z}{2} \cdot \sqrt{\left(\frac{\delta}{0.002}\right)^3 \cdot Dw} \tag{3}$$

$$\text{Cylindrical:} \quad F_{pal} = \frac{Z}{2} \cdot \left(\frac{\delta \cdot La^{0.8}}{0.0006}\right)^{\frac{1}{0.9}} \tag{4}$$

In the equations above, the displacements are introduced in $mm$ and the loads are obtained in $decaNewtons$. In the case of the models developed in the current research, the displacements are obtained from the FE node in $X$ and $Y$ so the forces are obtained in the same axes. The direction of the forces when expressed as vectors in the connectivity arrangement has to be matched with one of the relative displacements of the bearing races.

*2.2.2. Rolling bearing model considering the IAS perturbation approach*

The complete analytical description of this model was presented in reference [5] which should be consulted for detailed information. The present paper is limited to a synthesis of the hypothesis made to build such a model. The main idea is to split the rolling bearing into ball elements as seen in figure 2 and to compute for each position the loads applied on each ball and then the resulting load applied on each ring. Position of each ball can be defined by two angles : $\varphi$ and $\psi$.

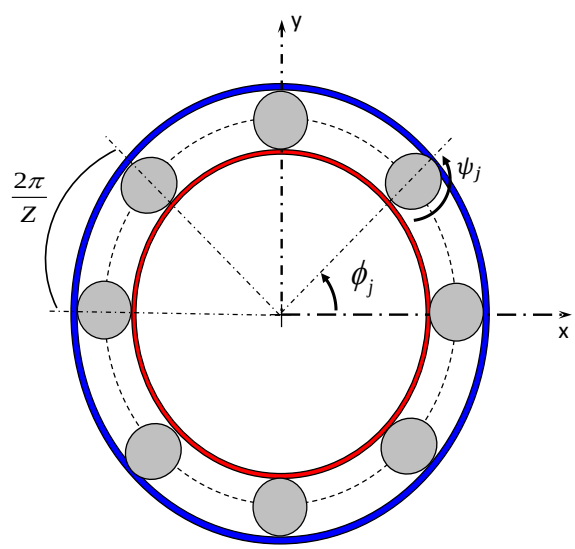


Figure 2: Ball bearing discretization

Firstly, rolling elements are assumed to roll without any slippage, thus allowing to express the position of the $jth$ rolling element as:

$$\begin{array}{rcll} \varphi_j & = & \varphi_{jo} + \theta_{IR} \cdot FTF & \qquad j = 1, 2...Z \\ \psi_j & = & \psi j0 + BSF.\theta_{IR} & \end{array} \tag{5}$$

where $\varphi_{jo}$ and $\psi_{j0}$ define the starting position of the $j^{th}$ rolling element and $\theta_{IR}$ is the angular position of the inner race. FTF is the Fundamuntal Train Frequency and BSF is the Ball Spin Frequency.
Considering the position of the rolling element as a function of the angle of the

inner race allows the approach to handle non constant angular speeds. The outer race rotation is considered to be fixed.

Secondly radial static equilibrium of the ball is assumed, that allows to compute the normal load $N$ applied on each ball. In this step, the introduction of a spall can be made by modifying the geometry of the races or the rolling elements which is equivalent to locally modifying the bearing clearance.
Then equations of dynamic motions of each ball are written (figure 3.a), they are a combination of two rotations $\varphi$, defined in equation 5, and $\psi$ corresponding to the spin rotation. Loads applied on ball $j$ are presented in figure 3.a.
At that step the normal load $N$ is known and the tangential loads $T_i$ and $T_e$ are unknown. The rolling resistance phenomenon is introduced. This complexity is needed to introduce the torque perturbations leading to the IAS variations induced by the bearing dynamics. Due to the rolling resistance phenomenon, the local deformation of the solids in contact by action of the external forces moves forward the point of application of the normal force [5] and introduces a torque into the rolling element (see Figure 3.b).

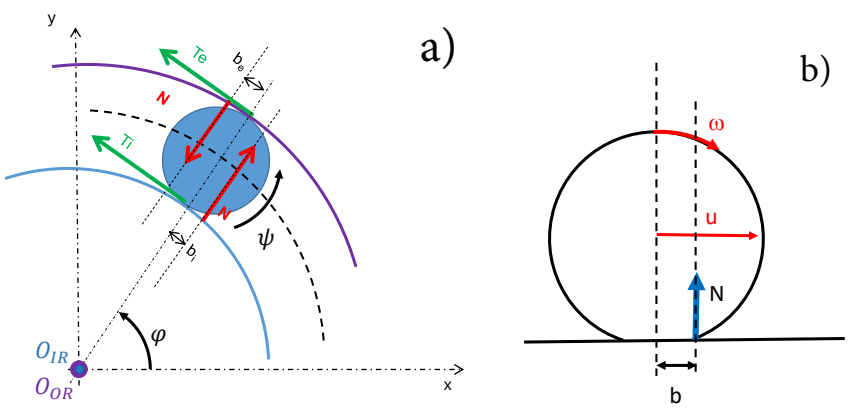


Figure 3: a) Loads acting on ball element - b) Rolling resistance phenomena

As detailed in [5] linking loads applied on the nodes $O_{IR}$ and $O_{OR}$ corresponding to the center of the inner and outer rings can be expressed in equation 6

$$[F_{link}]_{Bearing} = [F_{link}]_N + [F_{link}]_T + \ddot{\theta}_{IR}.[F_{link}]_\gamma \tag{6}$$

These vectors have force components along $x$ and $y$ axis and torque components along $\theta_z$. Vectors $[F_{link}]_N$, $[F_{link}]_T$ and $[F_{link}]_\gamma$ depend of the normal contact load $N$, of the mass, inertia of the ball element and of the BSF and BPFO of the bearing. $\ddot{\theta}_{IR}$ is the angular acceleration of the center of the inner ring.

Notice that since the forces and therefore the torques are a function of the normal force which varies as the rolling element goes in and out of the load zone, variations occur in the radial acceleration and angular speed, even for healthy bearings.

### *2.3. The gear mesh model and the angular approach*

The modeling strategy described hereafter is based on a very classic approach used widely in the literature. Since the analysis of the IAS response due to the bearing dynamics in non stationary conditions is of primary interest, explicit consideration of the angular DOFs is necessary. From a general point of view, gears are considered as rigid cylinders linked by restorative forces due to the paired gear stiffness representing the contribution of the ensemble of the deformable parts. Mass and inertia of the pinions are modelled using lumped parameters located on the nodes $O_1$ and $O_2$ corresponding to the center of each pinions. Describing the meshing of the gears as linking forces is similar to the approach of Bartelmus [8]. Main idea of this approach is that the load applied by the gear meshing on pinion i is equivalent as a punctual force $F_{gear}$ applied at the pitch point along the pressure line as shown in figure 4. Note that in this paper only the case of spur gear is considered.

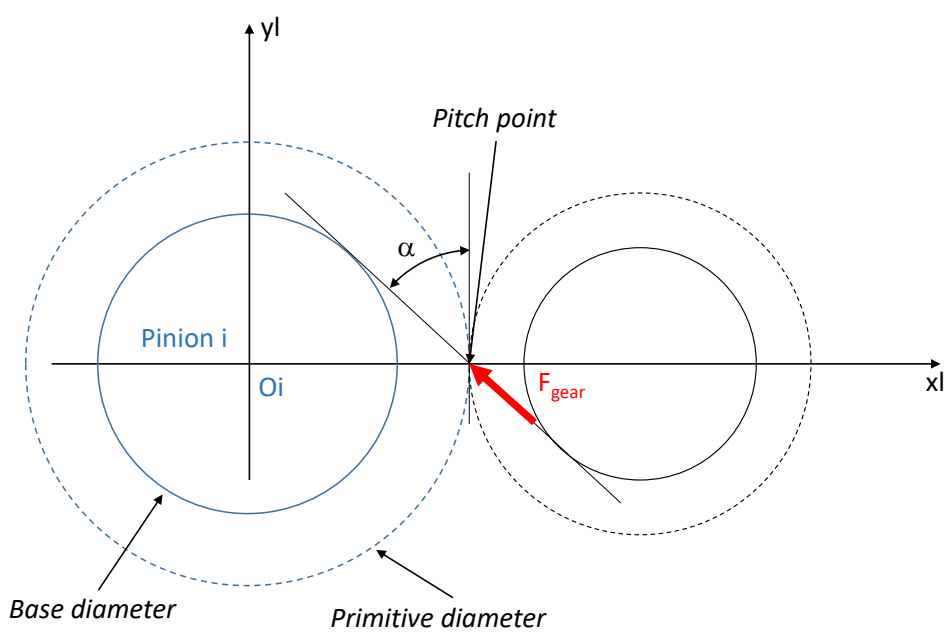


Figure 4: Gear load definition

Gear force can be estimated by:

$$F_{gear} = k_{gear}(\theta).\varepsilon_d(\{X\}) \tag{7}$$

Where $\varepsilon_d$ is the dynamic transmission error expressed along the pressure line and $k_{gear}$ is the gear meshing stiffness. In practice $k_{gear}$ is non constant as the number of acting tooth varies during meshing.

Regarding this work, to keep the signal simple for analysis of the IAS variations originated by the bearing dynamics, the choice has been made to consider the stiffness $K_{gear}$ as constant and equal to the teeth average stiffness. The ISO 6336 standard [13] empirical expression was used for the estimation of this parameter:

$$K_{gear} = 20 \cdot B \cdot 10^6 \qquad [N/m] \tag{8}$$

where $B$ represents the width of the paired gears.

Let $[X_{gear}]_L$ be the vector of displacements of nodes $O_1$ and $O_2$ expressed in the local base associated to the gear (Fig 4). The dynamic transmission error can be expressed as:

$$\varepsilon_d = \langle \sigma \rangle . \{X_{gear}\}_L \tag{9}$$

Where $\langle \sigma \rangle$ is a constant line vector depending of the gear geometry and can be expressed as:

$$\langle \sigma \rangle = \langle 1\,0\,0\,0\,0 \; -R_{b1} \; -1\,0\,0\,0\,0 \; -R_{b2} \rangle \tag{10}$$

Where $R_{bi}$ is the base radius of pinion $i$.
Note that one attempts that $\epsilon_d$ be positive. If it is not the case it's mean that the gear is not loaded or that the local base is not correctly defined (the contact flank is not correctly defined).
Then the linking force applied on node $O_1$ and $O_2$ expressed in the local base can be expressed as :

$$[F_{link}] = k_{gear}.^T \langle \sigma \rangle . \langle \sigma \rangle .[X_{gear}]_L \tag{11}$$

Let $[F_{link}]_{Gear}$ be the vector of gear linking forces expressed in the global base. It contains radial load, torque and bending moments.

### *2.4. System resolution in the angular domain*

Once the entire system is assembled for resolution it is arranged in form of state equations and transformed to the angular domain [5]. Principle is

described below. Using the linking forces defined above, global linking force vector is defined as:

$$\begin{aligned}[F_{link}([X])] &= \sum_{j=1}^{nb\,gear}[F_{link}]_{gear,j} + \sum_{j=1}^{nb\,Palm}[F_{link}]_{Palm,j} \\ &\quad + \sum_{j=1}^{nb\,Bearing}[F_{link}]_{N,j} + [F_{link}]_{T,j} + \ddot{\theta_{IR,j}}.[F_{link}]_{\gamma,j} \\ &= [F_{link}([X])]_1 + \sum_{j=1}^{nb\,Bearing}\ddot{\theta_{IR,j}}.[F_{link}]_{\gamma,j}\end{aligned} \tag{12}$$

Let $[Q]$ be the state vector :

$$[Q] = \begin{Bmatrix}[X] \\ [\dot{X}]\end{Bmatrix} \tag{13}$$

The equation (2) becomes

$$[\dot{Q}] = [A].[Q] + \begin{bmatrix}0 \\ [M]^{-1}\end{bmatrix}.\left([F_{ext}] + [F_{link}]_1 + \sum_{j=1}^{nb\,Bearing}\ddot{\theta_{IR,j}}.[F_{link}]_{\gamma,j}\right) \tag{14}$$

$\ddot{\theta_{IR,j}}$ is a component of $[\dot{Q}]$. Then it can be expressed as :

$$\ddot{\theta_{IR,j}} = \langle T_j\rangle.[\dot{Q}] \tag{15}$$

Where $\langle T_j\rangle$ is a line vector with a single non zero component. Then the dynamic problem becomes:

$$[\dot{Q}] = [A].[Q] + \begin{bmatrix}0 \\ [M]^{-1}\end{bmatrix}.\left([F_{ext}] + [F_{link}]_1 + \left(\sum_{j=1}^{nb\,Bearing}[F_{link}]_{\gamma,j}.\langle T_j\rangle\right).[\dot{Q}]\right) \tag{16}$$

$$\begin{gathered}\left([I] - \begin{bmatrix}0 \\ [M^{-1}]\end{bmatrix}.\left(\sum_{j=1}^{nbBearing}\{F_{link}\}_{\gamma,j}.\langle T_j\rangle\right)\left\{\dot{Q}\right\}\right) = \\ [A].\{Q\} + \begin{bmatrix}0 \\ [M^{-1}]\end{bmatrix}.(\{F_{ext}\} + \{F_{link}\}_1)\end{gathered} \tag{17}$$

$$[S].[\dot{Q}] = [A].\{Q\} + \begin{bmatrix}0 \\ [M^{-1}]\end{bmatrix}.(\{F_{ext}\} + \{F_{link}\}_1) \tag{18}$$

$$[\dot{Q}] = [S]^{-1}.[A].\{Q\} + \begin{bmatrix}0 \\ [M^{-1}]\end{bmatrix}.(\{F_{ext}\} + \{F_{link}\}_1) \tag{19}$$

Where $[A]$ is the state matrix defined by

$$[A] = \begin{bmatrix}0 & [I] \\ -[M]^{-1}.[K] & -[M]^{-1}.[C]\end{bmatrix} \tag{20}$$

As defined in [5] and [14], if the angular speed $\omega$ is still non-zero, this problem can be solved in the angular domain and becomes:

$$\frac{\mathrm{d}\{Q(\theta)\}}{\mathrm{d}\theta} = \frac{1}{\omega(\theta)}[S]^{-1}.[A].\{Q\} + \begin{bmatrix} 0 \\ [M^{-1}] \end{bmatrix}.(\{F_{ext}\} + \{F_{link}\}_1) \tag{21}$$

$$\frac{\mathrm{d}t}{\mathrm{d}\theta} = \frac{1}{\omega(\theta)} \tag{22}$$

The system of equations may be solved with conventional non linear resolution methods. In particular, after testing different Matlab ODE methods, the ODE15s happens to be more effective in computation time for the systems tested in this work. ODE15s Solve stiff differential equations with variable order method. But no numerical analysis has be performed to understand why it is the most effective as it is not the aim of this work.

## 3. Construction of a turbine model for testing surveillance indicators

### *3.1. Description of the wind turbine shaft line*

The wind turbine modeled is inspired by a machine instrumented by Andre et al. in [15] with an IAS acquisition system to perform an experimental study about IAS indicators. The machine is a MM82, built by Senvion, which produces 2 MW of electrical power when operating with wind speeds above 12 m/s. Such a machine has an 82 meter diameter rotor consisting of three blades attached to a rotating hub. The shaft line is situated at 80 meters of height inside the nacelle and is attached to a steel tower. The main components of the shaft line are the rotor, the Main Bearing, the speed multiplier gearbox and the generator. Figure 5 shows the disposition of these components in the wind turbine's nacelle. Notice that the shaft line axis has an inclination of $5^o$.

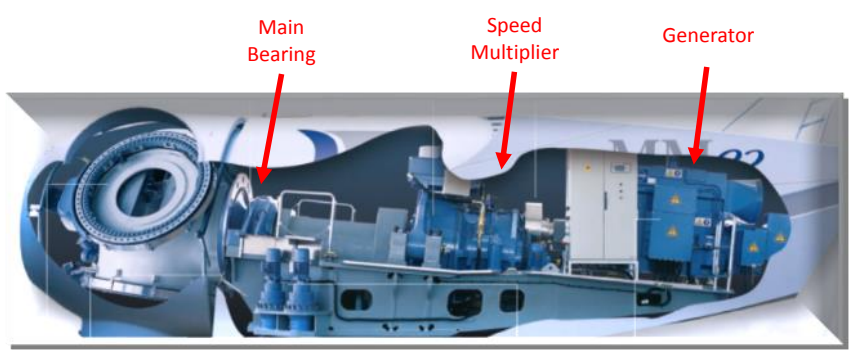


Figure 5: Parts of the MM82 wind turbine shaft line

The Main Bearing supports most of the rotor weight and represents a critical asset in these machines. For this study, Although other designs exist, the main

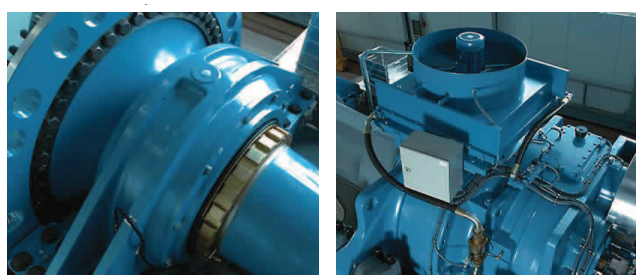

(a) Main bearing (b) Gearbox

Figure 6: MM82 Main Bearing and Gearbox

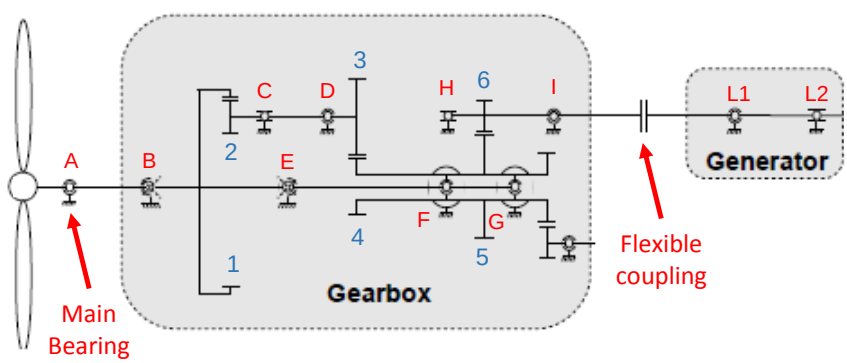


Figure 7: MM82 kinematics scheme

bearing is here modeled as a double row spherical bearing of 630 mm of inner race diameter (see Figure 6(a)).

The gearbox has three stages of combined planetary - helical gears (see Figure 6(b)). The nominal mechanical power is 2.225 MW and the gear ratio is around 105.5. Figure 7 shows the scheme of the kinematics of the whole wind turbine shaft line with the three stages of the gearbox. The first epicyclic stage has three planets (2) with a fixed planetary carrier which implies no sun gear and the input is through an internal ring gear (1) attached to the Low Speed Shaft. These planets are the input for the second epicyclic stage which has no ring gear and the output is through a sun gear (4) connected to all three planets and to the shaft leading to the last helical gear stage (5/6). The same intermediate shaft is the one motorizing the gearbox oil pump by means of a parallel spur gear stage. No reference to the mechanical efficiency is mentioned in the manufacturer's technical description. The ratio for each increasing stage are 4.429, 4.381 and 5.438.

The generator is doubly fed induction machine with a nominal power of

Table 1: Bearing characteristics of the shaft line

| Bearing | Characteristics |
|---|---|
| A | Double row spherical. Self-aligning |
| B | Single row tapered |
| C | Double row cylindrical |
| D | Double row tapered. Self-aligning |
| E | Single row tapered |
| F/G | Single row cylindrical |
| H | Single row tapered |
| I | Double row tapered |
| L1/L2 | Deep groove ball bearings |

Table 2: Main Bearing characteristic frequencies

| | Frequency (ev/rev) |
|---|---|
| BPFO | 12.75 |
| BPFI | 15.25 |
| BSF | 5.42 |
| FTF | 0.45 |

2080 kW at 1800 rpm. It has a speed range from 900 to 1800 rpm. A frequency converter is used for the control and regulation of the active and reactive power. It also recovers the rotor power from the generator.

The machine has also blade variable pitch and a yaw system as well as an installed encoder in the shaft end of the generator. These features allow to control different system configurations to obtain maximal electrical power generation depending of the wind direction and speed.

Among the different rotating components which are monitored by Engie Green (renewable energy company that develops and operates wind farms in France) with the IAS acquisition and analysis system, we find the complete set of bearings as well as the gears. Besides the main bearing, the machine has 9 rolling bearings inside the gearbox and two more rolling bearings supporting the generator shaft. The characteristics are shown in Table 1 identified with the labeling of Figure 7. Angular characteristic frequencies of the main bearing in events per revolution[16], on which is focus this work, are detailed in Table 2.

A flexible coupling links the gearbox and the generator and its primary function is to avoid mechanical deterioration caused by possible misalignment between these two components.

### *3.2. Construction of the MM82 simplified model*

Modeling the shaft line of the MM82 with the approaches presented in the previous sections demanded several simplifications. Figure 8 shows the resulting architecture of the mechanical system taking into account the simplifications described hereafter.

The two planetary stages of the gearbox were modeled as a cylindrical gear stage. The intermediate (or planetary and sun gear) shafts' inertia and mass were lumped into nodes 8 and 9 respectively which means that the effect of these shafts' flexibilities are not taken into account. Another important simplification is that no axial load is considered in the system, due to the fact that the rolling bearing models take into account the forces only in the radial and tangential directions. For this reason, all the gear teeth were considered straight. Neglecting the axial forces reduces the accuracy of the load distribution among the bearings which directly affects the dynamic response of the model and in consequence the IAS variations.

Regarding the dimensions, all gears have the same pitch diameter, modulus and width as of the represented gears. This choice leads to three modeled stages having the same transmission ratio as the real gearbox. The ring bearing inertia and mass were lumped into node 6 and the inertias and masses of all 6 planets were lumped into node 8.

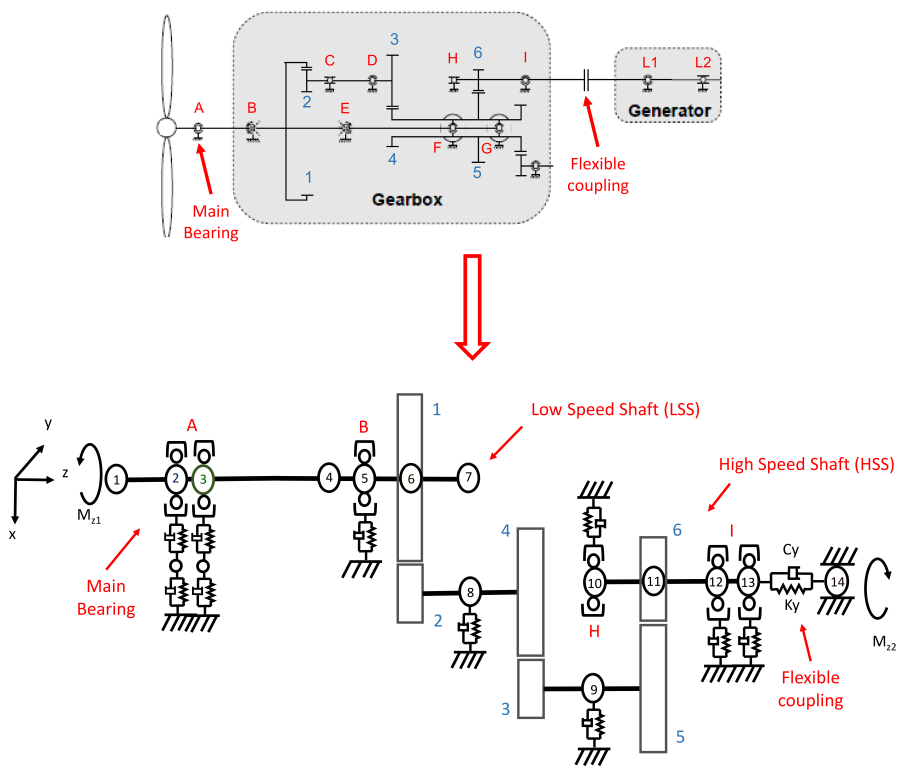


Figure 8: Simplified model architecture

The Low Speed Shaft (LSS), discretized into 7 nodes was geometrically trun-

cated until node 7 which is placed spatially in the center of what would be the bearing E. The High Speed Shaft (HSS), which is the output of the gearbox, was discretized into four nodes. Only four bearings were considered. In the LSS, only two bearings were modeled including the main bearing to avoid the hyperstaticity of the real architecture. Notice that the three bladed rotor and the ring gear (gear 1) are attached to the Low Speed Shaft meaning that no flexible coupling exits in the input of the gearbox. This shaft is very slender after the third bearing from left to right (Bearing E) and the bearings are not meant to support but to be a guide to align the shaft. The other two modeled bearings were those supporting the High Speed Shaft of the gearbox. The rotor inertia and mass are lumped into the node 1 and a static load equivalent to the rotor weight is applied vertically. This load represents most of the static charge supported by the Main Bearing.

The Main Bearing (bearing A), which is a double row spherical one, is described by the model of section 2.2.2 as a double row deep groove ball bearing. Therefore the response of the system expresses only the frequency characteristics of the load distribution dynamics and the geometry of this bearing. The diameter of the inner and outer races as well as the rolling element radius were considered identical to the real bearing. The other three bearings (bearings B, C and D) were modeled with the Palmgren equations. The nodes 8 and 9 representing the intermediate shafts were allowed to rotate in the three directions and they can also have displacements along the axes X and Y of the coordinate system in Figure 8, allowing the radial dynamics of the gear meshes to be translated to the whole shaft line.

The shaft of the generator was concentrated onto the node 14. This node is free to rotate in all directions and contains the inertia and mass of the generator's shaft and rotor. The flexible coupling is modeled as an external element linking nodes 13 and 14, with rotational stiffness and damping obtained from the manufacturer only in the Z direction. The choice of restraining node's 14 displacements was made to reduce the degrees of freedom of the system and to increase the stability for the convergence of the Matlab ODE solver method.

Reduced dynamic parameters of the Main Bearing's housing were obtained by analyzing its modal behavior. Two displacement degrees of freedom were retained for the X direction and one for the Y direction as presented in Figure 9.

For the rest of the bearings, only one displacement degree of freedom was considered for directions X and Y and the value was chosen with the same order of magnitude as the vibrational pads in which the Gearbox rests (See Figure 10(a)). Regarding the supports of nodes 8 and 9 representing the intermediate shafts, one degree of freedom by radial direction stiffness and damping elements were considered. For this particular case, the stiffness was overestimated to avoid convergence issues that were identified related to lumping the whole inertia and degrees of freedom of two gears into one node (See Figure 10(b).)

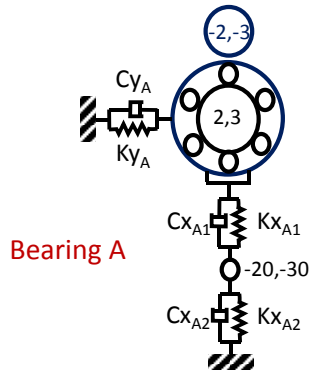


Figure 9: Support configuration for the Main Bearing

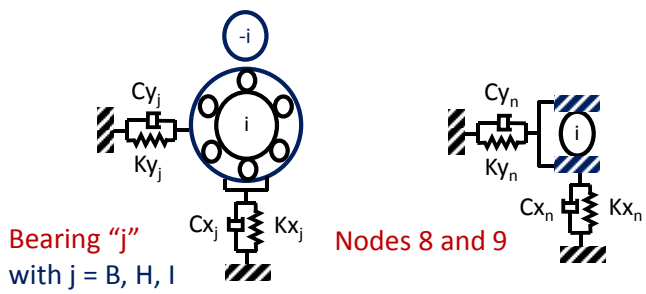


(a) Support configuration for bearings B, H and I

(b) Support configuration for nodes 8 and 9

Figure 10: Different bearing supports

### *3.3. The setup of the model*

This section describes the protocol used to perform non stationary simulations allowing to analyze the potential of the model as a tool to build and test condition monitoring spectral indicators.

The test of the IAS indicators comprised two major stages. The former was the setup of the model for simulations taking into account the evolution of a defect in the outer race of the main bearing. The second is the estimation of such spectral indicators and their treatment related to the non stationarity conditions.

#### *3.3.1. The design of non stationary simulations*

The objective was to obtain non stationary realistic simulations from the point of view of the operating conditions. To perform this task, data measured

by Engie Green often used to analyze machine performance and productivity have been utilized. From the model's point of view, the inputs needed, were basically the torque induced by the blades onto the rotor by action of the wind and the resistive torque induced by the generator into the High Speed Shaft.

The rotor torque is estimated by the following aerodynamic equation [17]:

$$T_{wind} = \frac{C_e \cdot \rho \cdot V_{wind}^3 \cdot \pi \cdot R_{rotor}}{2 \cdot \Omega_{rotor}} \tag{23}$$

where $\rho$ represents the air density, $V_{wind}$ is the wind speed and $R_{rotor}$ is the rotor radius. $C_e$ represents the non dimensional rotor power coefficient which is usually a function of the pitch angle, the rotor angular speed $\Omega_{rotor}$ and the wind speed. The coefficient is related to the Betz's law which establishes that the maximum power recovered by a wind turbine's rotor can not be greater than 60% of the kinetic power of the wind [18].

Figure 11 shows the operation parameters measured by Engie Green from a MM82 wind turbine identified as M1. The range of operation chosen was limited to wind speeds between 5.5 and 8 $m/s$. In this range, the generator's angular speed (Figures 11 and 12) has approximately linear behavior related to the Wind Speed.

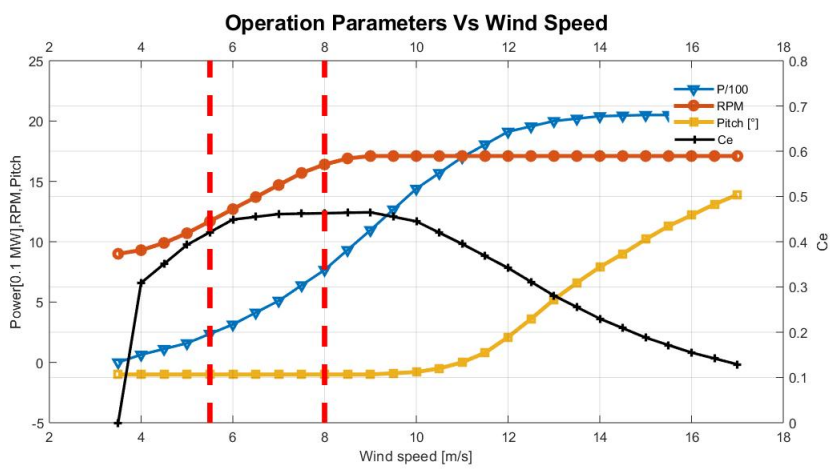


Figure 11: Measured operating parameters of a MM82

To simplify the analysis, the power coefficient was considered constant and equal to its maximum which is 0.49. It can be observed from Figure 11 that the variation of this coefficient in the wind speed range chosen is less than 15%. This consideration overestimates the value of the input torque and in consequence the load on the gears and bearings. The wind speeds were obtained from real measured data performed by Engie Green which are recorded with a sampling

frequency of 1 $Hz$.

Regarding the generator's resistive torque, the behavior was also obtained from Engie Green's measurement data base. The torque, measured on the generator's converter, is estimated as a function of the angular speed and is shown in Figure 12 for two different MM82 machines. Notice that the curves are very alike. The curve from the M1 machine between 1130 and 1750 rpm was approximated to a linear function with positive slope to be used in the simulations as the generator's torque curve. The resultant generator's resistive torque function $M_G$, is shown in Equation 24 where the angular speed $\omega$ has to be expressed in $rad/s$ and the torque is obtained in $Nm$.

$$M_G(\omega) = 45.66 \cdot \Delta\omega + 1100 \qquad [Nm] \tag{24}$$

where

$$\Delta\omega = \omega - \left(1130 \cdot \frac{2 \cdot \pi}{60}\right) \qquad [rad/s] \tag{25}$$

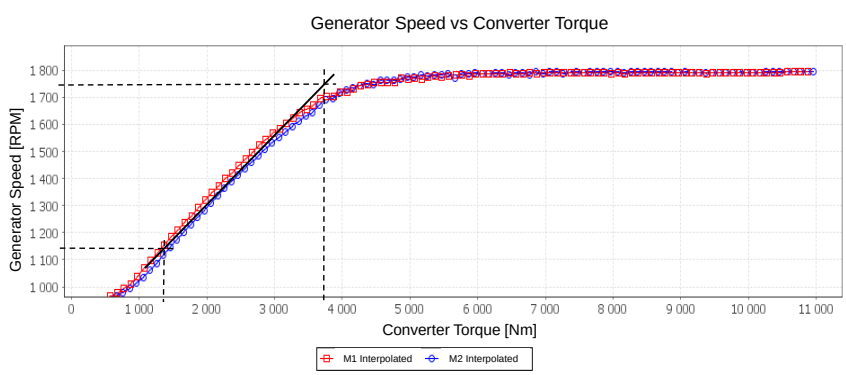


Figure 12: Measured converter torque of a MM82

Actually, an automated control system based on the measured parameters of wind speed and the generator's angular speed manages the operating condition response of the machine i.e resistive torque, pitch angle, etc.). In the case of the simulations, a basic control loop was built by means of the described equations to obtain the rotor and generator torques as a function of the wind speed. Figure 13 shows the resulting loop control for the mechanical model.

### *3.3.2. The visco-elastic angular damping coefficient and the response of the model to wind*

The damping coefficient $\nu$ was estimated for an angular speed of the generator of 1450 rpm which is around the middle of the range analyzed. Equation 23 was used to calculate the input torque at a wind speed of 7 $m/s$, value obtained

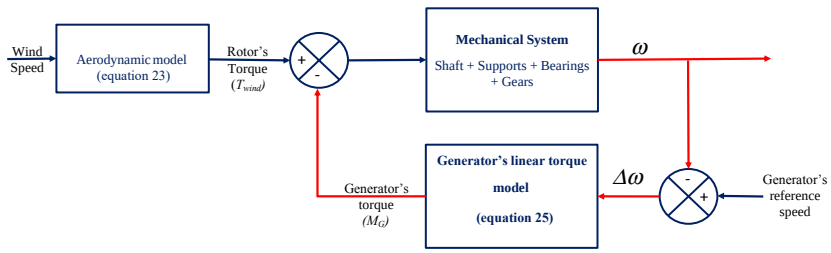


Figure 13: Control Loop for the Simulations

from the graph in Figure 11. Equation 24 was used as well to find the generator's resistive torque for this operating condition. The resulting value after iterations was set to 0.8 $Nms/rad$.

By performing simulation tests at the operating conditions of 1130 and 1750 rpm it was verified that the mechanical losses, produced by the mixture of the inner race resistive torque of the main bearing and the visco-elastic angular damping $\nu$, were of 4.5% and 10% respectively. These loses were estimated by the ratio between the power introduced by the rotor to the Low Speed Shaft and the power produced by the generator.

### *3.3.3. The evolution of the defect and the number of simulations*

In order to simulate a surveillance procedure, a number of measurements were simulated for healthy and defective bearings and in non-stationary conditions. To achieve this goal 200 non stationary simulations were run for a healthy machine and 200 with a defect seeded in the outer race of the Main Bearing for a total of 400 simulations. To achieve this task, 400 different wind speed measurements were used.

Table 3: Defect sizes evolution

| Defect size | Depth, $C_d$ $[\mu m]$ | Angular Length, $\Delta\phi_d$ [°] | Loading loss, % |
|---|---|---|---|
| D1 | 15.00 | 0.64 | 10 |
| D2 | 33.00 | 0.80 | 15 |
| D3 | 51.67 | 0.93 | 25 |
| D4 | 70.00 | 1.07 | 35 |
| D5 | 88.33 | 1.21 | 45 |
| D6 | 107.00 | 1.36 | 55 |
| D7 | 125.00 | 1.50 | 65 |
| D8 | 143.00 | 1.64 | 75 |
| D9 | 161.67 | 1.79 | 85 |
| D10 | 180.00 | 1.36 | 95 |

Regarding the faulted simulations ten different sizes of spall were parameterized simulating a damage evolution. The sizes are characterized by depth and length regarding the percentage of normal force loss when the rolling element

passes through the spall and the percentage of angular distance related to the angular spacing between two rolling elements (Figure 14). Thus, the smaller defect was set to a 5% of the angular length between the balls and 5% of normal force loss. The biggest one was set to 15% of angular spacing and 95% of loading loss. The defect was linearly increased in length and depth to achieve the ten different sizes. Table 3 contains the values for the depth and the length of the defect severity along with corresponding loading losses. Twenty different simulations were performed for 20 different wind speeds for each defect size for the total of 200 simulations with the faulted bearing.

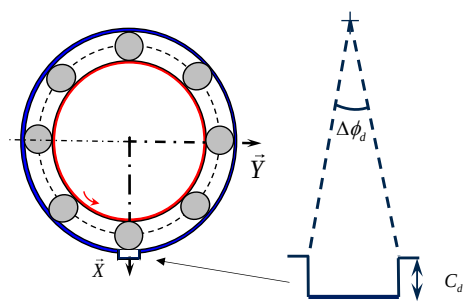


Figure 14: Defect representation, not scaled with the bearing's geometry

Figure 15 shows the evolution of normal force distribution between the rolling elements of the Main bearing, in presence of the defect sizes 1 and 10 with the HSS operating at 1450 rpm. Each curve represents the normal effort evolution of one rolling element passing through the load zone. Notice the increase of the load loss which is characteristic of the defect severity. Figure 16 focuses around one rolling element passage over the defect size 10, and shows clearly a sharp change in load distribution affecting of the rolling element crossing the defect (red curve) and its close neighbors.

### *3.4. The IAS surveillance indicators*

The indicator construction has two phases: the estimation based on spectral amplitudes and the normalization process allowing to make them independent of the operating conditions and to construct a model permitting the set of statistical defect thresholds.

#### *3.4.1. The spectral indicators*

Since the analysis is done on angular domain, frequency-smearing phenomenon is prevented and simple indicators based on amplitude on characteristic frequencies are more robust. In this work, five indicators are used for comparative studies, which are $S_{H1}$, $S_{H2}$, $S_{H4}$, $S_{H8}$ and $S_{H12}$ the spectral amplitudes at 1X, 2X, 4X, 8X and 12X the BPFO characteristic frequency. The five indicators have been chosen to be tested and compared with Experimental results from the data base in a machine carrying a defective bearing in the generator (Bearing L1).

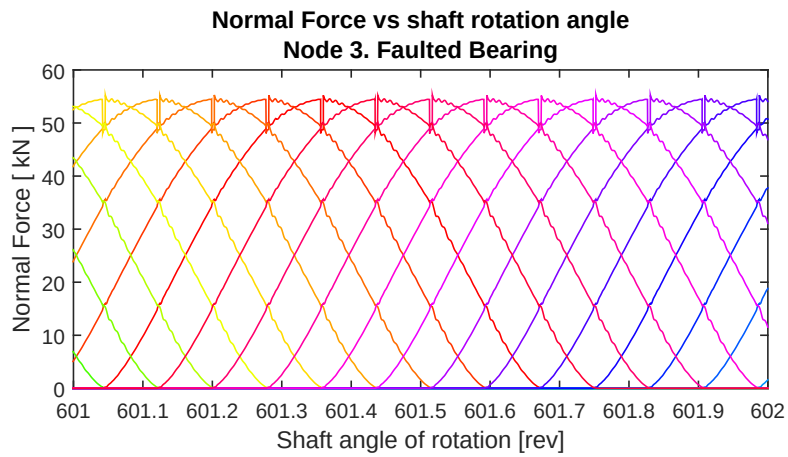


(a) Normal load distribution. Defect size 1

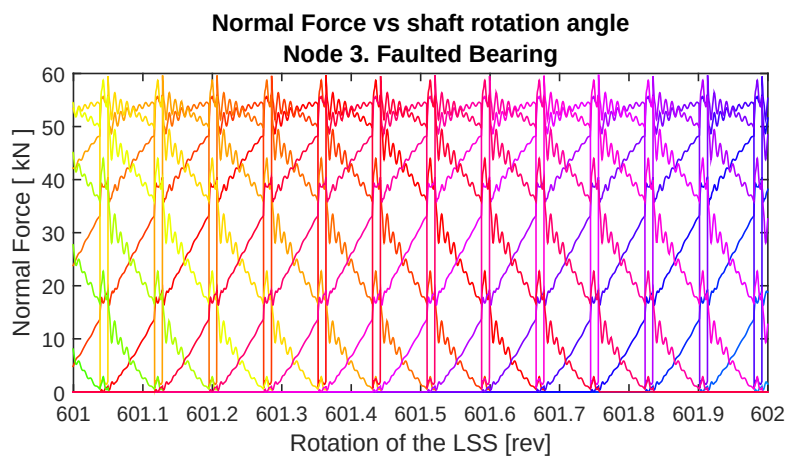


(b) Normal load distribution. Defect size 10

Figure 15: Normal load distribution of the Main Bearing. Node 3. Defect evolution

The angular response from the node 7 of the model was the one foreseen to be treated by a simulation of the encoder with elapse time method as in reference [14].

*3.4.2. The normalization procedure*

The normalization process is necessary to compare indicators obtained for different operating conditions, and is based on the assumption that indicators are following a conditional multivariate normal distribution: 'Conditional' since the monitored element, whose health status is noted $H$, is either healthy or defective. 'Mutlivariate' since several operating conditions $\mathbf{x}$ are also influencing the noise statistics $\mu$ and $\sigma$. Under these assumptions, the objective of nor-

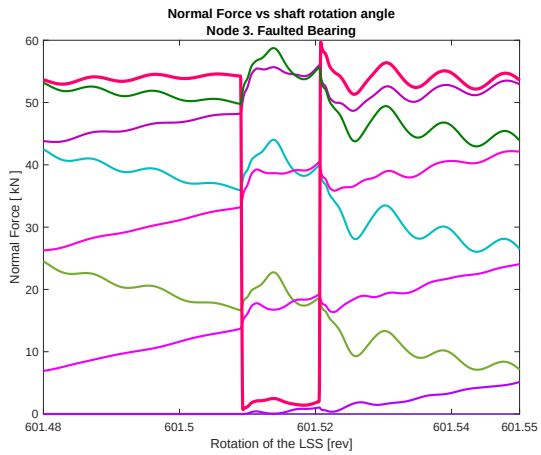


Figure 16: Zoom on normal load distribution, Defect size 10

malization is to estimate the function $f$ describing at best the law followed by the monitored indicator, which is symbolized by the random variable $I$ such as: $I = f(\mu(\mathbf{x}), \sigma(\mathbf{x})$ ass. $H)$. $f$ is assessed with a Support Vector Regression applied on a reference data base. This database is a compilation of healthy signals simulated under different and variable operating conditions. Support Vector Regression is chosen since the shape of function $f$ is completely unknown a priori and also to avoid extremely high computational costs usually linked with multivariate regressions. $\mu$ and $\sigma$ are respectively estimated using PRESS and CRPS criteria, in an iteration process tackling the heteroscedastic behaviour of data. Finally, the normalized indicator is computed such as: $I^{(n)} = \frac{I-\mu(\mathbf{x})}{\sigma(\mathbf{x})}$ and is expected to depend on the monitored element health status only.

Interested readers are invited to look at [19], [20] and [21] for details about Support Vector Regression formulation and adapation to vibration signals. The CPRS criterion used to estimate the variance is presented and detailed in [22].

## 4. Results and discussions

### *4.1. Stationary condition*

As it was described, the parameters of the model were adjusted to make the High Speed Shaft (HSS) to run at 1430 rpm under a constant wind speed of 7 $m/s$. The estimated rotor torque for this speed is 354.50 $kNm$ and the resistive torque is 3.20 $kNm$ for 480 kW of energy production.

The response of the IAS variation is shown in presence of the defect size 10 which is the most severe as it was described in the previous section. Notice that the Main Bearing has a $BPFO_\theta$ equal to 12.75 $ev/rev$.

The IAS variation is shown in Figure 17 for the nodes 7, 13 and 14. As expected, the shape and the amplitude of the variation changes depending on

the node analyzed. The authors have verified that the shape of the response therefore the energy distribution in the frequency channels of the spectra depends strongly on the modal response of the whole mechanical architecture. In this particular case, the $9 \cdot BPFO_\theta$ is found to be in the vicinity of a critical frequency. It can be seen in both the frequency and the physical domain, that the amplitude of the phenomena tends to be amplified by the transmission ratio. From measurements taken in the wind turbine that has been instrumented for [15], this phenomena may be observed for certain harmonics related to different mechanical cyclic events.

Another interesting observation is the redistribution of the amplitude of the IAS due to the mechanical coupling. This is easily corroborated by comparison of the IAS spectra of the nodes 13 and 14 (Figures 17(d) and 17(f)). The coupling seems to filter the phenomena and it makes the fundamental frequency's peak higher than the others reorganizing the energy distribution when compared to node 13 where the harmonics starting from the 4th have more amplitude.

### *4.2. Indicator analysis in stationary conditions*

A preliminary analysis of the spectral response in healthy conditions and in presence of defect sizes 1, 5 and 10 has been done. The spectra shown in Figure 18 were obtained from the virtual encoder of the Low Speed Shaft placed in node 7. A logarithmic scale has been set to improve the observation of the first harmonics. We can notice the presence of peaks at the fundamental and harmonics even in healthy case which are usually masked with surrounding noise in experimental measurements. The amplitude of peaks tends to increase with the evolution of the defect size. Not all harmonics react the same way regarding defect size increase. We can also notice a slight variation in the shape of the spectra. It's also observed that the presence of the defect increases the energy around the harmonics linked to the BPFO of the bearing but this phenomena was not further investigated.

With the aim of doing a comparison with experimental results, a similar analysis was made for one deep groove ball bearing outer race defect detected by the maintenance team of Engie Green, in the generator of a MM82 which happened to be equipped with encoders on the HSS and the LSS, as described by André et al. in [23]. The results presented for this machine are from the HSS encoder which is installed on the same shaft as the damaged bearing at the end of the generator driving shaft. The IAS Signals were acquired using the elapse time method [24].

As a first step, three IAS signals were analysed: the former extracted about one month before the replacement (Defect level 1); the second, one the day before the replacement (Defect Level 2) and the last one, a few days after the replacement of the bearing (Healthy). The three signals were chosen as they are in the same range of speed and load and they present low macroscopic speed fluctuation. IAS Signals have the particularity that they contain information from the whole kinematic line of the machine, in fact low energetic phenomena related for example to bearings dynamics could be masked by high energetic ones. In order to keep focus on the bearings related components in spectra,

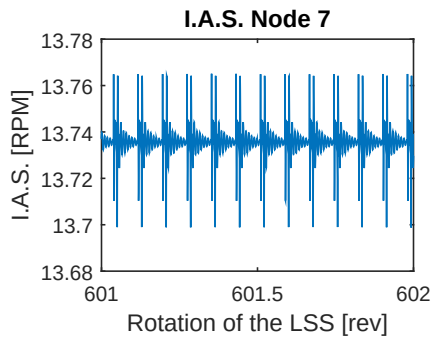


(a) IAS. Node 7. Faulted Bearing

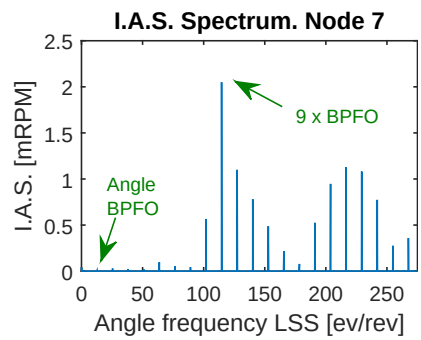


(b) IAS Spectrum. Node 7. Faulted Bearing

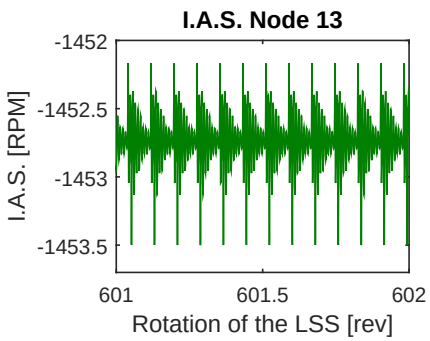


(c) IAS. Node 13. Faulted Bearing

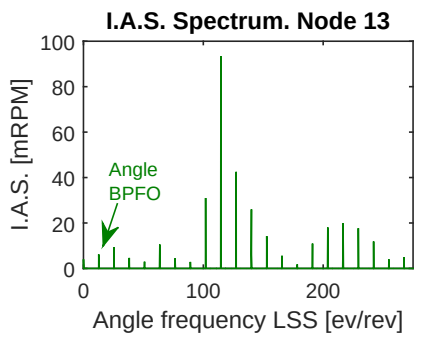


(d) IAS Spectrum. Node 13. Faulted Bearing

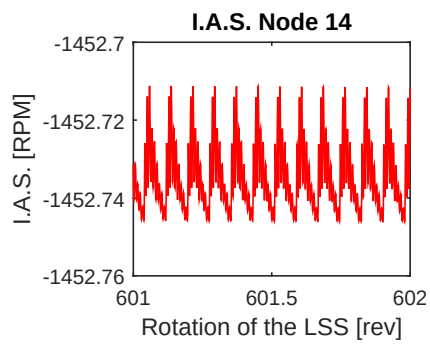


(e) IAS. Node 14. Faulted Bearing

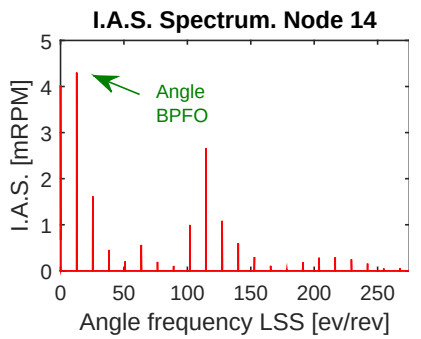


(f) IAS Spectrum. Node 14. Faulted Bearing

Figure 17: IAS response for nodes 7,13 and 14. Faulted bearing

all frequency components relative to gear transmission were simply removed. Figures 19 show spectra obtained after removal of gear transmission components. The first harmonic of BPFO can be seen in both healthy and defective signals

with similar amplitudes. On the other hand, much higher amplitudes of higher harmonics of BPFO are seen in the case of the defective bearings. Similarly to what is observed with the signals generated by the model, side-bands around the BPFO fundamental frequency and its harmonics are also observed, but only in the defective cases. This phenomenon requires further investigation to determine its origin and its possible use for failure detection.

$S_{H1}$, $S_{H4}$ and $S_{H12}$ Indicators described in section 3.4.1 were extracted from the spectra shown above. Figure 20 shows the levels of the extracted indicators from experimental and modelled measurements, for the healthy bearing, and for different levels and sizes of bearing defects as shown on spectra 18 and 19. The presence of a small defect in modelled signals makes the $S_{H1}$ indicator decrease relative to the healthy bearing. A decrease is also observed for this indicator between defect sizes 2 and 3. A similar observation can be seen for the case of experimental signals where the amplitude of the indicator on Dl1 is smaller than its value for the healthy case. The indicator $S_{H4}$ seems a more stable indicator, as a slight increase is notified on Ds1 and Ds2 for modelled signals and in Dl1 for experimental signals. A bigger amplitude is seen on final stage Ds3 and Dl2. The indicator $S_{H12}$, seems more efficient as early detection is observed, in fact, the gap between the healthy and defective cases is seen from the least severe state (Ds1 for modelled signals and Dl1 for experimental ones).

The experimental results are similar to the modelled ones in terms of the sensitivity of the indicator to the presence of the defect. Regarding the $S_{H1}$ indicator, similar phenomena to those observed in reference [5] occurs: the presence of a small defect make the H1 indicator decrease relative to the healthy bearing. The obvious conclusion is that the fundamental frequency is not a good indicator for bearing surveillance. The indicator $S_{H12}$ is more sensitive to the defect evolution. The sudden variation in load distribution in the rolling elements due to the rotation of the shaft, highly amplified in the presence of a defect, may be the cause for the higher harmonics to respond more to the defect evolution. As the excitation behaves as successive impacts, it excites the critical frequencies of the system coupling both phenomena.

### *4.3. The non-stationary simulations*

To show the model response in non stationary conditions one of the simulation runs for the indicator testing is shown in Figure 21. The first results presented are in presence of the Main Bearing's defect size 10 and are treated by the virtual encoders placed in nodes 7 and 14 of the model measuring LSS and HSS angular speeds respectively.

Figure 21(a) shows the input wind speed which transformed into rotor torque, drives the mechanical system. Notice that the linear response of the simulated generator's linear control loop makes the system respond with an angular speed that has the same shape as the wind. In reality, the wind turbine control is not quick enough to keep such linearity between wind speed and angular speed.This exagerated reactivity accentuates torque and load variations onto gears and bearings. Hence, low frequency regions of the IAS spectram are poluted by sharper macroscopic speed variations than usually observed in reality.

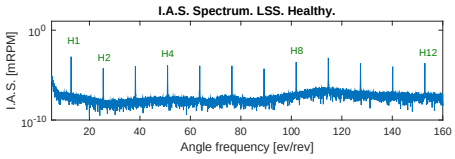


(a) IAS Spectrum. Encoder in LSS. Healthy Main Bearing.

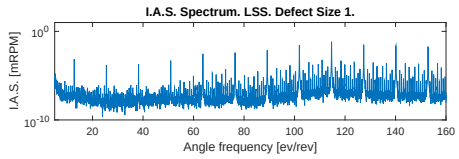


(b) IAS Spectrum. Encoder in LSS. Defect Size 1.

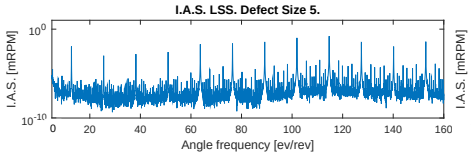


(c) IAS Spectrum. Encoder in LSS. Defect Size 5.

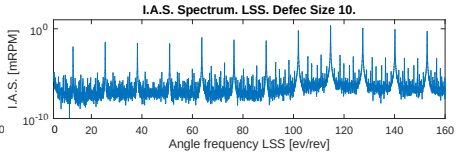


(d) IAS Spectrum. Encoder in LSS. Defect Size 10.

Figure 18: IAS logarithmic spectra evolution in presence of a Main Bearing defect. Stationary condition.

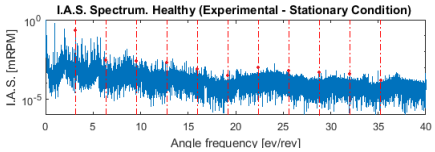


(a) IAS Spectrum. Encoder in HSS. Healthy Bearing.

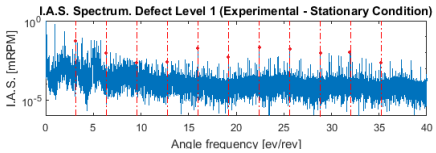


(b) IAS Spectrum. Encoder in HSS. Defect level 1.

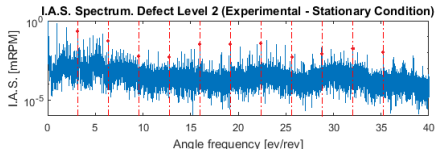


(c) IAS Spectrum. Encoder in HSS. Defect level 2.

Figure 19: IAS logarithmic spectra evolution in presence of a High speed shaft Bearing defect.Experimental - Stationary condition.

However, spectra obtained the simulated signals do not show significant differences related to the ones simulated in stationary conditions in terms of the energy distribution between the frequency channels (See Figure 17). This means that the speed variation does not make the modal response change significantly. However, a great difference in the amplitudes is observed as the non stationary spectra present smaller peaks.

To have a better observation Figure 22 shows the spectra in logarithmic scale for the LSS encoder of one simulation example for defect sizes 1 and 10. The non stationary spectra show a broadband effect in the low angle frequency

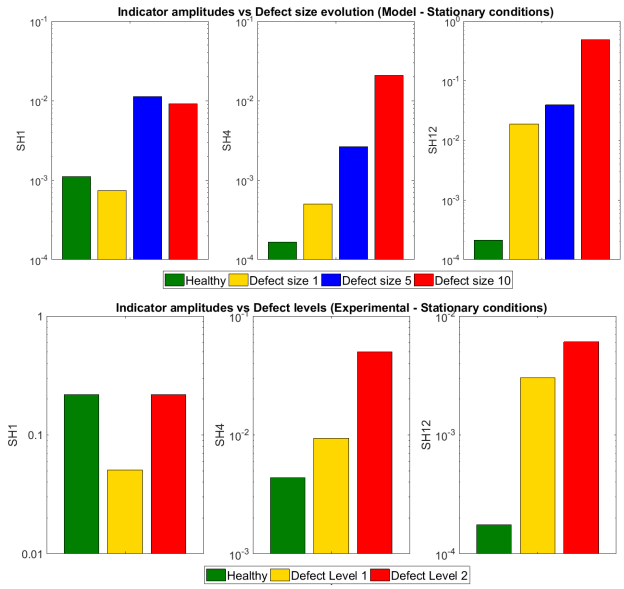


Figure 20: IAS indicators vs Defect evolution

region caused by the transitory dynamics of the response related to wind as well as a clearer observation of the modal excitation in the region between 100 and 150 $ev/rev$. The critical frequency excitation moves from the H8 to the H9 in the observed spectra. The range of speeds set for normalization will make this frequency move no more than two harmonics.

It can be noticed that the broadband noise hides the first three harmonics related to the bearing dynamics in the case of the defect 1. This implies that in the case of the model, using these peaks as a part or as a whole indicator in non stationary conditions would make early detection more difficult. In the case of the defect size 10, a general increase of the amplitudes is observed and the energy introduced by the big size of the bearing defect makes the first harmonics stand out from the noise.

### *4.4. Indicator analysis in non stationary conditions. Comparison with experimental results*

The normalization procedure described in section 3.4.2, was applied to the 400 simulations, 200 in healthy conditions of the Main Bearing and 200 in faulted conditions following the procedure developed in Section 3.3.3.

Back now to the experimental machine, the normalization procedure was applied based on the same indicators and with the very same parameters as it was performed for the model. However, as the analysis is made on a real bearing failure, there is no control on the defect evolution. The measurements used to build the parametric law are from the period immediately after the bearing's replacement to ensure the healthy bearings condition.

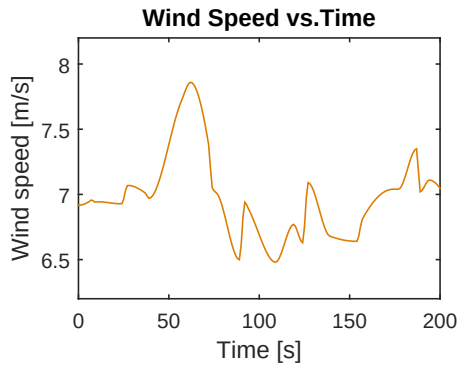


(a) Wind speed vs time

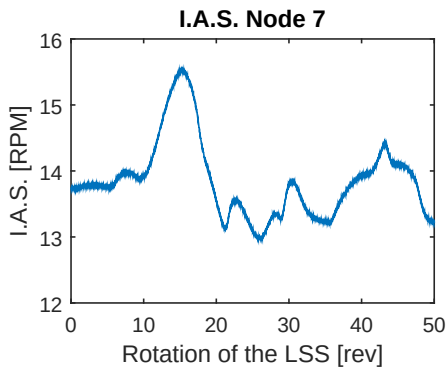


(b) IAS. Encoder in Node 7. Faulted Bearing

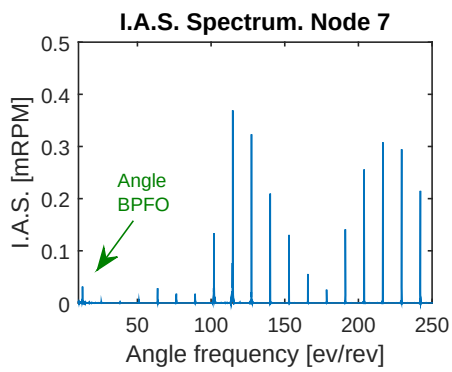


(c) IAS Spectrum. Encoder in node 7. Faulted Bearing

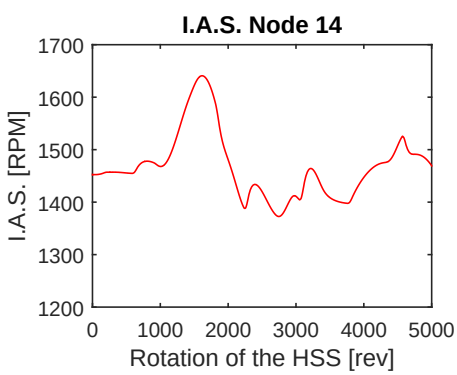


(d) IAS. Encoder in Node 14. Faulted Bearing

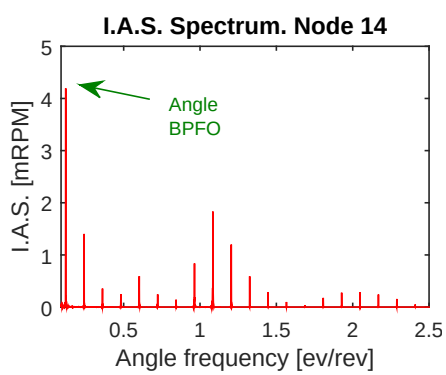


(e) IAS Spectrum. Encoder in Node 14. Faulted Bearing

Figure 21: Non stationary IAS response in presence of a Main Bearing defect. LSS and HSS modeled encoders

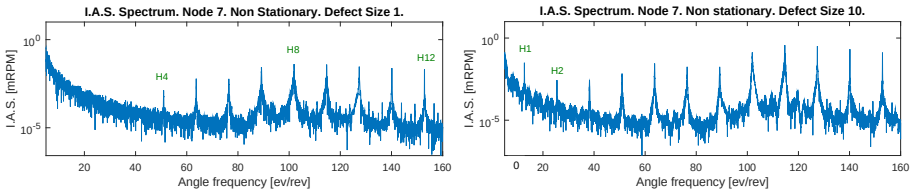


(a) IAS Spectrum. Encoder in node 7. Defect Size 1. Non stationary conditions

(b) IAS Spectrum. Encoder in Node 7. Defect Size 10. Non stationary conditions

Figure 22: IAS logarithmic spectra in presence of defect sizes 1 and 10. Non stationary conditions.

The experimental measurements belong to a period of six months and they are taken at a rate of around 20 measurements per day. Nevertheless, only those satisfying the range of angular speeds between 1130 and 1750 rpm were considered to match the set up for the simulations as described in Section 3.4.2.

It is important to remark that the operating conditions for the simulations, induced by the wind speed measurements, are not related with the conditions of the real machine in the period of measurements. This makes the results interesting from the point of view of the random selection of the conditions for the model related to the experimental data. Having common operating conditions would have been more important if the objective of the model was to accurately reproduce the machine's behavior.

Figure 23, presents the normalized indicators H1 and H12 for the model simulations as well as for the experimental results from the HSS encoder.

The indicator alarm has been set up to 5 standard deviations .Regarding the model simulations, each indicator point was labeled with sample number, giving a total of 200 samples for healthy condition and 20 samples for each defect size.

The blue data corresponds to the simulations with a healthy Main Bearing and the red data corresponds to the faulted bearing at a severity rate augmentation of one defect size every twenty simulations. When looking at the results (Figures 23(a) and 23(b)), it is confirmed that the indicator H1 does not respond well in terms of early detection. In contrast, each single estimated indicator H12 exceeds the alarm level.

In the case of the experimental results (Figures 23(c) and 23(d)), the presence of the bearing defect is identified by the value of the indicators related to the alarm line. Several measurements per day are taken as it can be noticed. The vertical dot line on the left of the plots points out the detection date of the defect by the maintenance team by means of vibration measurements and the dot line on the right establishes the moment of the bearing replacement. As it is the case for the results of the model, the indicator H1 "reacts" to the defect almost one month after the detection by radial vibration surveillance, but the presence of the defect is not clear as the average (black curve) is around the alarm value. Regarding the H12 indicator, the average clearly exceeds the alarm at almost the same date as the defect detection. Notice however that the

average goes beyond the alarm level several times in the period between the end of September and the beginning of December, which may be interpreted as a sign of early detection of the defect.

Figure 24 shows a comparison between all five analyzed indicators for both simulated and experimental results. The colored scale has been set to turn into yellow when the alarm of five standard deviations is reached. The maximum value is established to 320, as an indicative value and it does not represent the maximum value of the analyzed indicators. The intention of these plots is to offer a way to compare the sensitivity of the indicators related to the severity of the defect.

Regarding the model results it can be observed that indicators H4, H8 and H12 are very sensitive to the defect as they "react" for the defect size 1 which represents a very small pit. It is clearly observed that the indicator H12 is more sensitive to the defect severity as it reaches the biggest amplitudes.

From the experimental results, we have a similar behavior related to indicators H8 and H12 that happens to respond much earlier than the others. When comparing the results with the model it is confirmed the already mentioned similarity in terms of the trending and defect sensitivity.

In both, model and experimental results, the indicator H2 seems not to be suitable for surveillance. For the model results, when looking at figure 20, showing the evolution of this indicator in stationary conditions, the not normalized amplitude seems to be smaller in general than the H1 except for the defect size 10. It was observed from the spectral observations in non stationary conditions (Figure 22), that in general the spectral amplitudes are smaller compared to those obtained in constant angular speed which probably causes H2 not to respond after normalization, phenomenon shown in Figure 24(a). For the experimental results, it can be seen from Figure 24(b) that it responds erratically and only at the end of the faulted condition period which could be related to high variance of the normalized indicator.

In summary, the effectiveness of the indicators to detect the defect is the same for the experimental and the modeled results. The higher harmonic indicators respond first to the defect and in the same order (H12, H8, H4, H1 and H2) for the model as well as for the experimental results. Also, the higher normalized indicator amplitudes are obtained for H12 and H8 in both cases. These similar tendencies occur even if the evolution of the simulated defect has been made only from the point of view of the size and not in the sense of the spreading into the other components i.e. inner race and rolling elements, as well as extended or multiple size defects coexisting in the same race, which is what happens in reality and it would be expected to change the indicator's response.

Besides, the major simplifications made to build the model didn't seem to affect the similarity between the experimental and the simulated results. The simplifications are expected to affect in a high degree the modal response of the system and in less degree, but still important, the load on the bearings and the gears.

Finally, it can be stated from the results that more complex indicators composed of several bearing harmonics (sum, multiplication, etc) would be expected

to be very effective for bearing defect detection for IAS surveillance analysis in stationary and non stationary conditions.

## 5. Conclusions and perspectives

Throughout this work a simplified wind turbine model was presented based on the angular approach by considering the free rotation of the shafts. The model, inspired by a 2 MW wind turbine was built taking into account the same number of speed increasing stages as the real wind turbine. Experimental data of the wind speed and the active power generation was used to build non stationary simulations serving to test spectral indicators as a way to show the potential of the modeling approach.

The rigid body stationary response for a HSS angular speed of around 1430 rpm was confirmed validating the rigid body behavior of the system in free rotation. An indicator's preliminary analysis in stationary conditions, was performed in which it was observed that using the fundamental frequency amplitude as an IAS spectral indicator for bearings in the case of outer race defects does not seem suitable as it sometimes decrease with increase in the defect severity. It was observed that the higher harmonics tend to be more excited due to the bearing dynamics in presence of the defect which is coupled to the modal response of the whole mechanical architecture.

Regarding the non stationary response of the model, the angular speed follows exactly the same non stationary behavior as the wind, which is not what occurs in reality. The complex machine control was linearized in the model and this choice generates more dynamics in the transitory response which in consequence, increases the broad band effect in the low frequency range of the IAS spectra. This, tends to underestimate the detection of the first harmonics related to the bearing dynamics.

The indicator normalization procedure was used to perform the analysis of the indicators in the non stationary domain for the model results as well as for the experimental data obtained from a bearing defect detected in a wind turbine instrumented for IAS surveillance. From the model results as well as for the experimental indicators, it was found that higher harmonics are more sensitive to the presence of the defect. The difference in the responses between the model and the real wind turbine due to the simplifications, and the raw handling of the defect severity evolution did not seem to affect the above described similar tendencies in the indicator responses.

A fair compromise was found between the levels of abstraction and details chosen during the construction of the model and the generation of operating conditions (realistic speed and load variations based). This fair balance allowed us to obtain from model simulations global indicators whose evolutionary trends agree adequately with the experimental ones. The results show the robustness of the approach and promise easy adaptation to kinematics other than that used for demonstration

These results point to deepening the research in the construction of more complex indicators taking into account the higher harmonics of the defect fre-

quency by performing mathematical combinations of them. Also, deepen the exploration of techniques such as the spectral envelope applied to the IAS signal stands out as one of the perspectives of the current research to take advantage of the sensitivity of the IAS signal to the mechanical parameters of the system.

Finally, the wind turbine model served to show the potential of the angular approach. It allowed to test data analysis techniques showing similar tendencies between the model and the experimental results in spite of the simplifications. Further analysis has to be made to quantify the impact of the simplifications considered in this work.

## Appendix A. Effect of the rigid body angular damping on the angular response of a one DOF system

An illustrative example is used here to evoke the impact of the angular damping in a rotating system. Figure A.25 shows a scheme of a rigid body of inertia $J$ rotating with angular speed $\omega$ by action of the external moment $M$ applied in the direction of the angular DOF $\theta$. The angular speed $\omega$ is defined by:

$$\dot{\theta} = \omega \tag{A.1}$$

The equation describing the rotation of the body is:

$$J \cdot \frac{d\omega}{dt} + \nu \cdot \omega = M \tag{A.2}$$

Analyzing the system in the steady state condition, which means no angular acceleration, we observe that the constant angular speed is a function of the external torque and the mechanical losses represented by the angular rigid body damping:

$$\omega = \frac{M}{\nu} \tag{A.3}$$

Logically in an ideal system with no losses, meaning $\nu$ equal to zero, the angular speed will rise linearly as a function of time by action of the moment $M$:

$$\int_0^t J \cdot \frac{d\omega}{dt} dt = \int_0^t M dt \tag{A.4}$$

operating:

$$\omega = \frac{M}{J} \cdot t + \omega_o \tag{A.5}$$

As an example the mass inertia of the system is set to $2.70 \cdot 10^{-4}\ kg \cdot m^2$ and the moment applied is made equal to 15 Nm. The response of the system is analyzed by being solved with Matlab's ODE15 solver with an initial condition of the speed of 10 rad/s. The response is analyzed with no losses and with an angular rigid body damping of 0.15 Ns/m.

Substitution of the numerical data in Equation A.3 gives a steady state speed of 100 rad/s. Figure A.26 shows the response obtained by numerical integration and it can be observed that the system reaches, as expected, the theoretical steady state value for the angular speed.

Regarding the system with no damping, Figure A.27 shows the angular speed response after integration of the general equation. It can be observed that the linear response predicted by Equation A.5 is obtained. It can be verified, for example that the angular speed at 0.01 s is predicted to be equal to 664.50 rad/s which is exactly what is seen in the figure.

Notice that the steady state angular speed of the system is a function of this damping and it can be use to adjust the desire operating conditions of a given mechanical model.

## References

## References

[1] P. McFadden, J. Smith, Model for the vibration produced by a single point defect in a rolling element bearing, Journal of Sound and Vibration 96 (1) (1984) 69–82.

[2] D. Brie, Modelling of the spalled rolling element bearing vibration signal: An overview and some new results, Mechanical Systems and Signal Processing 14 (3) (2000) 353–369.

[3] A. Rafsanjani, S. Abbasion, A. Farshidianfar, H. Moeenfard, Nonlinear dynamic modeling of surface defects in rolling element bearing systems, Journal of Sound and Vibration 319 (35) (2009) 1150–1174.

[4] N. Sawalhi, R. Randall, Simulating gear and bearing interactions in the presence of faults: Part i. the combined gear bearing dynamic model and the simulation of localised bearing faults, Mechanical Systems and Signal Processing 22 (8) (2008) 1924 –1951.

[5] J. L. Gomez, A. Bourdon, H. André, D. Rémond, Modelling deep groove ball bearing localized defects inducing instantaneous angular speed variations, Tribology International 98 (Supplement C) (2016) 270 – 281.

[6] S. Singh, U. G. Kopke, C. Q. Howard, D. Petersen, Analyses of contact forces and vibration response for a defective rolling element bearing using an explicit dynamics finite element model, Journal of Sound and Vibration 333 (21) (2014) 5356 – 5377.

[7] H. D. Nevzat H., Özgüven, Mathematical models used in gear dynamics. a review, Journal of Sound and Vibration 121 (3) (1988) 383 – 411.

[8] W. Bartelmus, Mathematical modelling and computer simulations as an aid to gearbox diagnostics, Mechanical Systems and Signal Processing 15 (5) (2001) 855 – 871.

[9] W. Bartelmus, F. Chaari, R. Zimroz, M. Haddar, Modelling of gearbox dynamics under time-varying nonstationary load for distributed fault detection and diagnosis, European Journal of Mechanics - A/Solids 29 (4) (2010) 637 – 646.

[10] W. Bartelmus, Gearbox dynamic multi-body modelling for condition monitoring under the case of varying operating condition, Journal of Coupled Systems and Multiscale Dynamics.

[11] P. Velex, M. Ajmi, On the modelling of excitations in geared systems by transmission errors, Journal of Sound and Vibration 290 (3 - 5) (2006) 882 – 909.

[12] A. Palgrem, Les roulements: Description, théorie et applications, S.K.F., 1967.

[13] Iso 6336: Calculation of load capacity of spur and helical gears (2006).

[14] A. Bourdon, H. Andre, D. Remond, Introducing angularly periodic disturbances in dynamic models of rotating systems under non-stationary conditions, Mechanical Systems and Signal Processing 44 (1) (2014) 60–71.

[15] H. Andre, D. Remond, A. Bourdon, On the use of the instantaneous angular speed measurement in non stationary mechanism monitoring, in: ASME 2011 International Design Engineering Technical Conferences and Computers and Information in Engineering Conference, American Society of Mechanical Engineers, 2011, pp. 15–24.

[16] D. Remond, J. Antoni, R. Randall, Editorial for the special issue on instantaneous angular speed (ias) processing and angular applications, Mechanical Systems and Signal Processing 44 (1 - 2) (2014) 1 – 4, special Issue on Instantaneous Angular Speed (IAS) Processing and Angular Applications.

[17] S. Santoso, H. T. Le, Fundamental time domain wind turbine models for wind power studies, Renewable Energy 32 (14) (2007) 2436 – 2452.

[18] T. Burton, D. Sharpe, N. Jenkins, E. Bossanyi, Wind energy handbook, John Wiley & Sons, 2001.

[19] J. McBain, M. Timusk, Fault detection in variable speed machinery: Statistical parameterization, Journal of Sound and Vibration 327 (3–5) (2009) 623–646.

[20] H. Drucker, C. J. C. Burges, L. Kaufman, A. Smola, V. Vapnik, Support vector regression machines, in: Proceedings of the 9th International Conference on Neural Information Processing Systems, NIPS'96, MIT Press, Cambridge, MA, USA, 1996, pp. 155–161.

[21] H. Drucker, C. J. C. Burges, L. Kaufman, A. J. Smola, V. Vapnik, Support vector regression machines, in: M. C. Mozer, M. I. Jordan, T. Petsche (Eds.), Advances in Neural Information Processing Systems 9, MIT Press, 1997, pp. 155–161.

[22] E. P. Grimit, T. Gneiting, V. J. Berrocal, N. A. Johnson, The continuous ranked probability score for circular variables and its application to mesoscale forecast ensemble verification, Quarterly Journal of the Royal Meteorological Society 132 (621C) (2006) 2925–2942.

[23] H. André, A. Bourdon, D. Rémond, Instantaneous Angular Speed Monitoring of a 2MW Wind Turbine Using a Parametrization Process, Springer Berlin Heidelberg, Berlin, Heidelberg, 2012, pp. 415–423.

[24] H. André, F. Girardin, A. Bourdon, J. Antoni, D. Rémond, Precision of the ias monitoring system based on the elapsed time method in the spectral domain, Mechanical Systems and Signal Processing 44 (2014) 14 – 30, special Issue on Instantaneous Angular Speed (IAS) Processing and Angular Applications.

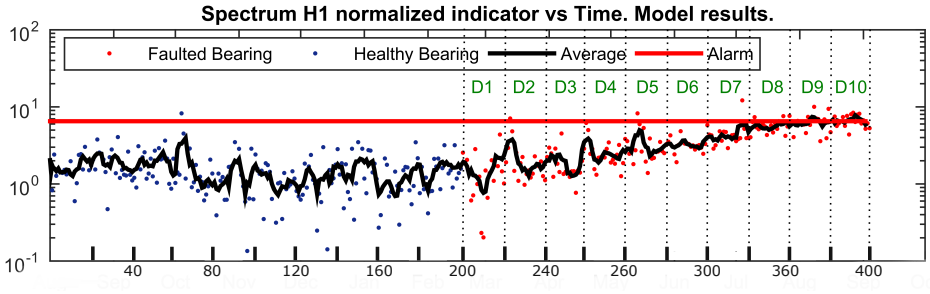


(a) IAS H1 Normalized indicator. Wind turbine model.

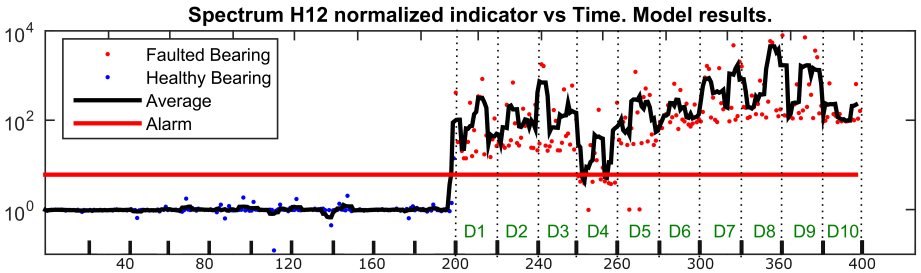


(b) IAS H12 Normalized indicator. Wind turbine model.

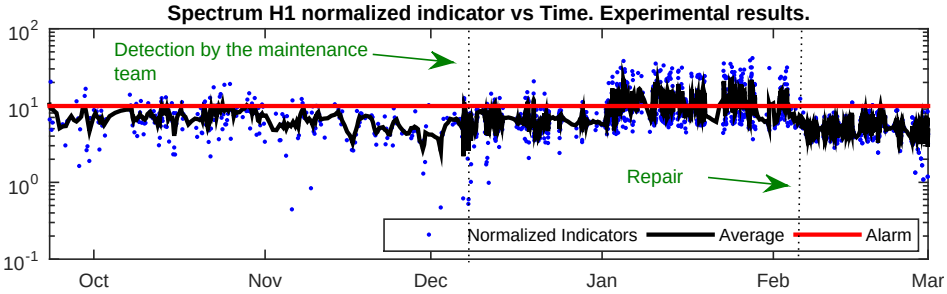


(c) IAS H1 Normalized indicator. Experimental results.

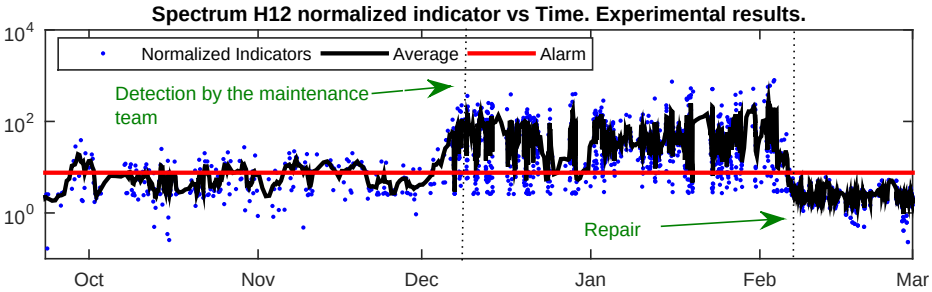


(d) IAS H12 Normalized indicator. Experimental results.

Figure 23: IAS normalized indicators H1 and H12. Modeled and experimental results.

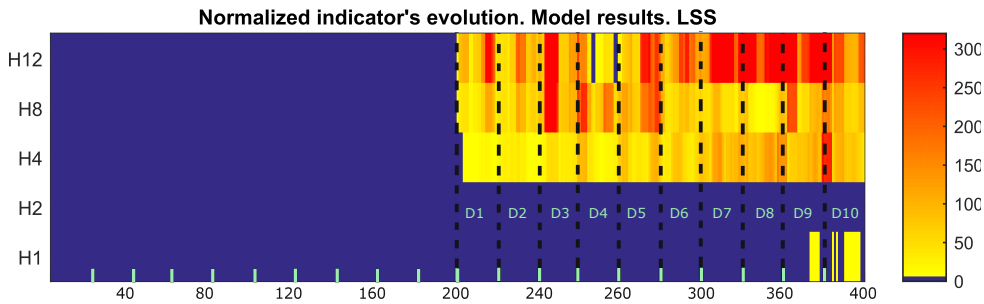


(a) IAS Normalized indicators comparison. Wind turbine model.

(b) IAS Normalized indicators comparison. Experimental results.

Figure 24: IAS normalized indicators comparison. Modeled and experimental results.

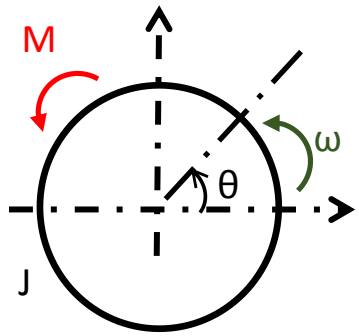


Figure A.25: General representation of single stage gear system

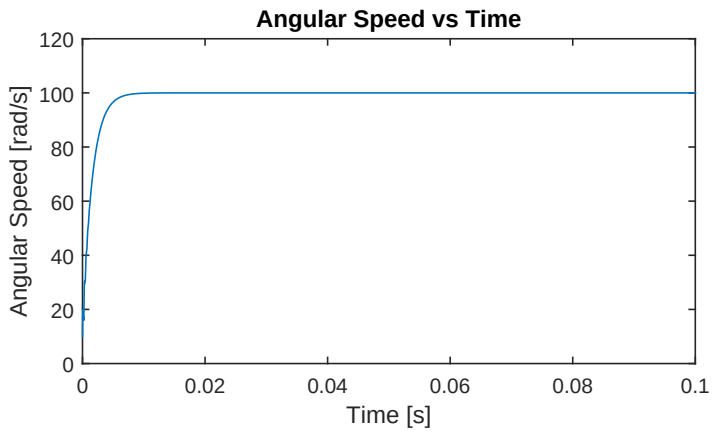


Figure A.26: Angular Speed response with rigid damping

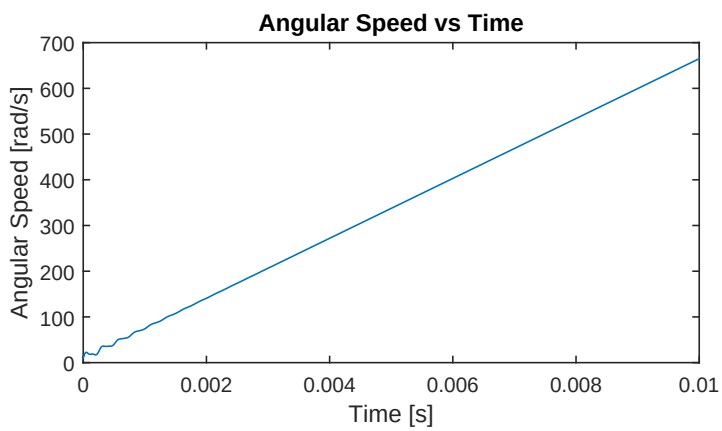


Figure A.27: Angular Speed response without angular loses

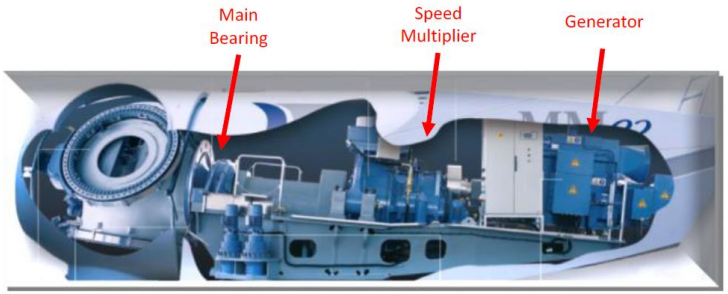


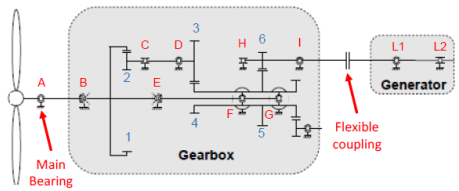


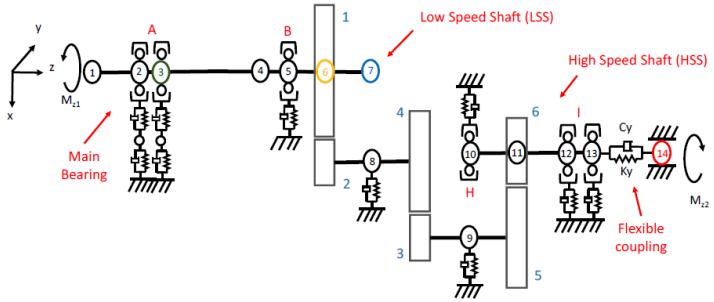


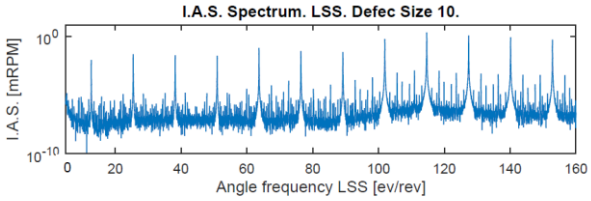


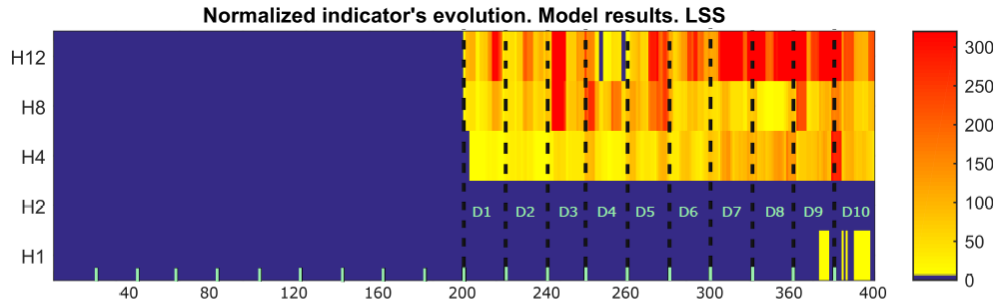


(a) IAS Normalized indicators comparison. Wind turbine model.

(b) IAS Normalized indicators comparison. Experimental results.